YALE
PEABODY
MUSEUM

JOURNAL OF MARINE RESEARCH

The *Journal of Marine Research,* one of the oldest journals in American marine science, published important peer-reviewed original research on a broad array of topics in physical, biological, and chemical oceanography vital to the academic oceanographic community in the long and rich tradition of the Sears Foundation for Marine Research at Yale University.

An archive of all issues from 1937 to 2021 (Volume 1–79) are available through EliScholar, a digital platform for scholarly publishing provided by Yale University Library at https://elischolar.library.yale.edu/.

Requests for permission to clear rights for use of this content should be directed to the authors, their estates, or other representatives. The *Journal of Marine Research* has no contact information beyond the affiliations listed in the published articles. We ask that you provide attribution to the *Journal of Marine Research.*

Yale University provides access to these materials for educational and research purposes only. Copyright or other proprietary rights to content contained in this document may be held by individuals or entities other than, or in addition to, Yale University. You are solely responsible for determining the ownership of the copyright, and for obtaining permission for your intended use. Yale University makes no warranty that your distribution, reproduction, or other use of these materials will not infringe the rights of third parties.

Langmuir supercells on the middle shelf of the South Atlantic Bight: 1. Cell structure

by D. K. Savidge[1,2] and A. E. Gargett[3,4]

ABSTRACT

Langmuir circulation cells extending through entire water columns exert a profound influence on sediment transport on shallow shelves, hence their designation as "Langmuir Supercells" (LSs) upon discovery in 2004 in water of 15 m depth at the Long-Term Ecosystem Observatory (LEO) off New Jersey (United States). Until now, similar high-frequency, full water column measurements of turbulent velocities and density fields have not been reported from significantly deeper continental shelf environments. Such deeper measurements are needed to determine whether LSs exist to influence sediment transport outside the inner shelf. In this article, that deficiency is addressed, using measurements from a midshelf location in the South Atlantic Bight. These data indicate that LSs form during high wind and wave forcing in water of 26 m depth and are thus capable of affecting sediment transport over more than about half of the area of this wide, shallow shelf. Relative to those at LEO, the LSs reported here are less organized and more temporally variable despite similar magnitude forcing. Possible causes of cell weakness and variability are considered.

Keywords: Langmuir supercells, shelf circulation, sediment transport processes

1. Introduction

Langmuir supercells (LSs) are Langmuir circulations that extend throughout the water column during high wind and wave events on shallow shelves. They were first discovered and described from observations at the Long-Term Ecosystem Observatory (LEO), a cabled observatory in water of 15 m depth on the continental shelf 7 km off the coast of New Jersey (Gargett et al. 2004). The three-dimensional velocity structure of the counterrotating cell pairs characteristic of Langmuir circulation (Langmuir 1938) was observed directly in high temporal resolution data from a five-beam 1,200 kHz acoustic Doppler current profiler, the vertical beam acoustic Doppler current profiler (VADCP). The name "supercells" was chosen to highlight the importance of these features to transport of suspended sediment on

1. Skidaway Institute of Oceanography, 10 Ocean Science Circle, Savannah, GA 31411.
2. Corresponding author: *e-mail: dana.savidge@skio.uga.edu*
3. Institute of Ocean Sciences, 9860 W. Saanich Rd., Sidney, BC V8L 4B2, Canada.
4. Department of Ocean, Earth and Atmospheric Sciences, Center for Coastal Physical Oceanography, Old Dominion University, 4111 Monarch Way, 3rd Floor, Norfolk, VA 23508; *e-mail: gargettann@gmail.com*

shallow shelves. Large vertical velocities associated with organized full-depth Langmuir cells during supercell events move wave-mobilized sediment out of a thin ocean bottom boundary layer (Trowbridge and Agrawal 1995) and distribute it high into the water column where storm-forced along-shelf mean velocities transport it over long horizontal distances. Sediment populations of sessile diatoms on some shallow shelves (Cahoon, Laws, and Thomas 1994; Nelson et al. 1999; McGee, Laws, and Cahoon 2008) suggest that sediments thus transported may contain diatom colonies and whatever organic detritus has rained down and escaped recycling on the shelf prior to the onset of LS events. Additionally, the end of supercell events is a mechanism for reestablishment of sorted sediments on shelves, as heavier fractions are first to fall out of the water column when cells begin to weaken.

Given the importance of supercells to the fate of both sediments and bioactive materials on shallow shelves, it is essential to determine the shelf depths to which they can extend, hence the percentage of shelf areas affected. However, the question of maximum possible depths to which full-depth Langmuir cells exist as supercells has remained largely unexplored. Indeed, since the initial discovery of LS in water of 15 m depth at LEO, no reports of such full-depth Langmuir circulations in appreciably deeper water columns have been published.

For example, Kukulka et al. (2011) reported acoustic measurements in the upper 3 m of a 16 m water column approximately 3 km south of Martha's Vineyard, Massachusetts, finding banded structures in the horizontal when mean current and wind directions were approximately collinear. Near-surface and near-bottom density measurements indicated very low stratification, so Langmuir cells at full water depth were likely to have accompanied the near-surface banded structure, given the low turbulent Langmuir numbers estimated. Such verification of limited stratification is crucial because of the sensitivity of LSs to even weak stratification (Gargett, Savidge, and Wells 2014). Variability of the near-surface wind-aligned banded structures was also observed and modeled under observed magnitudes of crosswind flow and shear. This exploration of the effects of crosswind currents on Langmuir circulations is relevant to the observations reported here and is discussed subsequently. Note that the measurements of Kukulka et al. (2011) were in water of essentially the same depth as the original LEO observations; hence, they do not contribute to the question of the maximum depth range to which LSs may exist on continental shelves.

In a subsequent study, Miles, Glenn, and Schofield (2013) examined glider data taken along the 40 m isobath off the coast of New Jersey during a period of strong winds from the northeast. As winds and waves increased, vertical velocities (determined from time rate of change of glider pressure, uncorrected for vehicle response) increased in frequency and magnitude throughout the water column, the water column became unstratified, and water column backscatter increased. These features are consistent with the presence of LSs. Though Miles et al. (2013) did not speculate on a causal link between those features and the existence of full-depth Langmuir cells at 40 m depth, they did conclude that LSs were not a likely cause of spatial heterogeneity in suspended sediments observed. We note that the

horizontal spatial sampling by the gliders, as operated, would have been too coarse to define typical horizontal cell sizes of LSs, estimated as two to five times the water depth (H) from the LEO observations. Therefore, the glider data cannot verify whether LSs existed during these operations along the 40 m isobath.

Finally, Scully et al. (2015) report on data from a depth of 14 m in Chesapeake Bay. This study provides an excellent review of model results and expected disruptions of Langmuir cells in shallow water relevant to their full-depth observations. Their findings indicate that despite strong vortex forcing, full-depth Langmuir cells seldom occurred, if at all, because of strong salinity stratification in the bay. Mixed buoyancy and vortex forcing both contributed to upper ocean turbulence. The findings reinforce the need for full-depth hydrographic information to assess the level of ambient stratification. In any event, the observations of Scully et al. (2015) at 14 m are no deeper than those at LEO.

It thus remains the case that there are no comprehensive observations of the full three-dimensional velocity field of LSs over the full water column depth in water deeper than that at LEO. Yet because of the profound influence of LSs on suspended sediment motion, the maximum depth that supercells can reach and hence the areal extent of the coastal ocean they can affect are questions of major importance. Are supercells limited to the inner shelf, or can they exist on the middle or outer shelf?

The observations reported here contribute to examination of this issue. Starting in 2007, observations similar to those at LEO were initiated at the U.S. Navy's R2 tower, in 26 m of water on the midshelf off Georgia in the South Atlantic Bight (SAB; the region between Cape Canaveral and Cape Hatteras on the East Coast of the United States). The SAB continental shelf off Georgia is approximately 100 km wide and extends to a 60 m deep shelf break (Jahnke et al 2008): the R2 tower is located 65 km offshore (Fig. 1). During measurements over several months in 2007, full water column backscatter events similar to those seen at LEO were observed at R2 during high wind and wave conditions (Fig. 2). A series of articles have described the characteristics of LSs as observed at LEO (Gargett et al. 2004; Gargett and Wells 2007), contrasted these shallow ocean features and Langmuir turbulence in the surface layer of the deep ocean (Gargett, Savidge, and Wells 2014; Grosch and Gargett 2016), and elucidated the forcing conditions that produce them (Gargett and Grosch 2014). Using the variety of analysis methods derived in those publications, along with the R2 tower observations of in-water turbulence and surface forcings, the R2 events will be shown to be LS events (Section 3).

Differences are noted between observations at LEO and at R2, in both the degree of organization of the Langmuir cells and in temporal variability relative to the stronger steadier cells at LEO (Section 3d). Kukulka et al. (2011) noted variations in the near-surface banded structure both as functions of the strength of wave forcing and of the crosswind tidal currents. Discussion of their results are deferred to Section 4, which examines possible causes of the differences detected in the deeper water column at R2. Of the two mechanisms hypothesized by Kukulka et al. (2011), the "cell-shearing" variety is shown to be the most likely contributor. Section 5 summarizes and concludes the article.
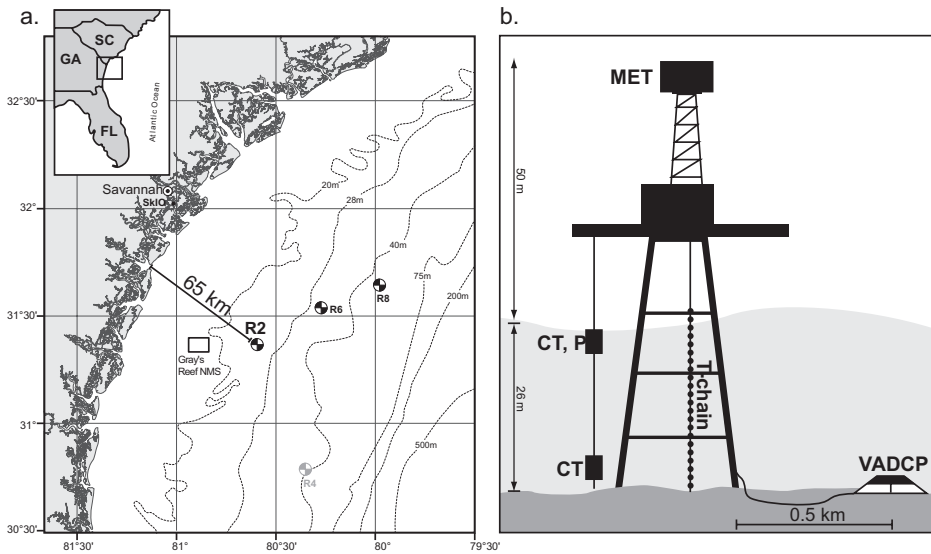
Figure 1. Study site and instrumentation. (a) South Atlantic Bight Synoptic Ocean Observatory Net-
work (SABSOON) of instrumented Navy towers on the South Atlantic Bight shelf, including R2 at
the 26 m isobath. (b) Schematic of instrumentation at R2. A vertical beam acoustic Doppler current
profiler (VADCP) was mounted on a pipe jetted into the sandy sediments ∼0.5 km east-southeast
of the tower, leveled by divers so that the vertical beam was within 0.6° of vertical and cabled to
the tower. An internally recording 1 m resolution Temperature chain (T-chain) provided continu-
ous temperature stratification information. These assets were embedded within existing SABSOON
instrumentation at R2: a meteorological package (MET) near-surface and near-bottom conductivity-
temperature (CT) packages, and a near-surface pressure gauge (P). Gray's Reef National Marine
Sanctuary (NMS) is shown.

2. Data and processing

a. Turbulence data

The information on the large-eddy structure of turbulence examined in this study was
obtained from a cabled 600kHz VADCP (RDI, San Diego, CA.). This was a custom-built
instrument with four slant beams and a fifth vertically oriented beam from a full-size (same
as the four slant-beams) transducer mounted outside the pressure case between transducer
faces 2 and 4 and cabled to a second set of control hardware within the instrument pres-
sure case. Slant beams were oriented at 30° from the vertical for improved resolution of
horizontal velocities: optimization of the trade-off between beam separation and beam ori-
entation is discussed in Gargett, Tejada-Martínez, and Grosch (2009). All five beams were
synchronized and sampled at 1 Hz. Bin size was 0.95 m, and the bin nearest the bottom
started at 1.6 meters above bottom (mab) (bin center at 2.6 m; in what follows, bin center
depths are rounded to the first decimal place). To avoid tower wake effects during normally
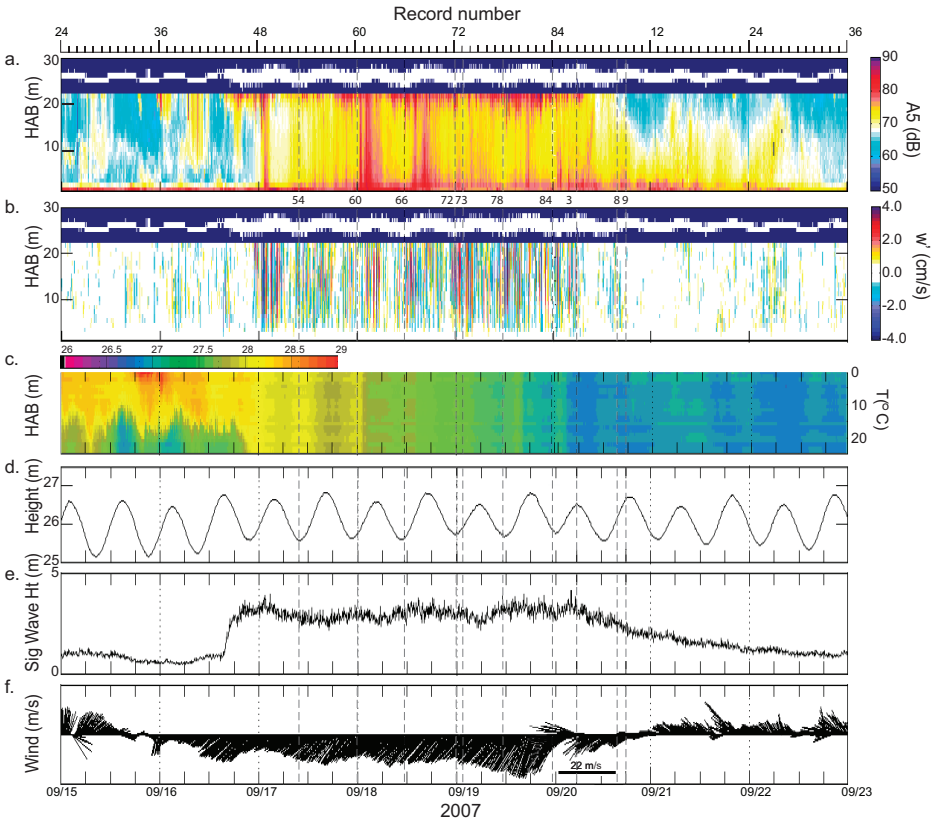
Figure 2. High wind and wave event recorded at R2, September 2007. Vertical beam acoustic Doppler current profiler (VADCP) data were subdivided into approximately 7-day sessions, subdivided and sequentially numbered into 2 h records. Shown are session 17, records 46–84, and session 18, records 1–36, 15–23 September 2007 (record numbers marked at the top). Panels are backscatter (a) and vertical velocity (b) from the VADCP fifth beam, with surface location (white) as identified in vertical beam backscatter; temperature evolution (c); low-frequency plus tidal water depth variation (d); significant wave height (e); and vector wind at 50 m (f). Panels a,b,c plotted as a function of height above bottom (HAB) in m.

northeasterly storm winds, the VADCP was deployed ∼0.5 km east-southeast of the R2 tower, to which it was cabled for communication and power. Beam data were recorded on a computer housed above sea level in the tower's air-conditioned control space and transferred to land via microwave link provided by the U.S. Navy. Data were divided into approximately 7-day "sessions" and each session was further subdivided and sequentially numbered into 2 hr "records"; individual records are referenced as, for example, 17.74. Processing steps included identification of the sea surface in fifth vertical beam backscatter, elimination of data at that level and above in the vertical beam (hence the vertical beam measurement

closest to the surface is centered at a depth of ∼0.5 m, half the bin size), and elimination of slant beam data in the upper 15% of water column, where it could be contaminated by side-lobe pickup of the surface. VADCP backscatter from the fifth beam has been corrected for beam spreading and absorption, but not calibrated to size or concentration of reflectors in the water column. A fish identification algorithm adapted from that used by Gargett and Wells (2007) was used along each beam to flag data contaminated by the presence of fish. Short temporal gaps were filled by fitting second-order polynomials vertically in each beam.

Because a spectral gap was maintained between the wave-band frequencies and frequencies of the predominant turbulent ocean structures examined here (see Appendix), a simple low-pass filter eliminates wave-induced velocities from the VADCP data without the need for alternative wave decontamination techniques (e.g., Kirincich and Rosman 2011). Beam velocities in each bin were filtered using a ninth-order low-pass Butterworth filter with cutoff frequency of 0.1 the Nyquist frequency, effectively retaining frequencies lower than 0.05 Hz with 0.1 Hz sample interval. For ease of expression, "10s" is used in discussions of these data. Horizontal velocities are calculated from slant beam data according to standard methods (Kosro 1985; Lohrmann, Hackett, and Røed, 1990), whereas vertical velocities are measured directly by the fifth vertical beam, accurately adjusted to vertical by a diver during deployment. To examine high-frequency variability in the VADCP velocity data, tide and mean current are removed from each 2 h 0.1 Hz time series by a linear least-squares fit to radial (beam) velocity components.

b. Auxiliary data

Meteorological data were available from a package mounted on the R2 tower at 50 m above the sea surface, as part of the South Atlantic Bight Synoptic Ocean Observatory Network (Seim 2000). Instruments included an anemometer (R.M. Young, Traverse City, MI) for wind speed and direction, relative humidity and air temperature sensors (Rotronics, Hauppauge, NY), an barometric pressure (IntelliSense, Woburn, MA), and shortwave and longwave radiation sensors (Eppley, Newport, RI). All instruments were operated continuously and recorded averaged values over 6 min intervals.

Wind stress was estimated by first converting wind speeds measured at 50 m to 10 m using the method of Smith (1988) and then converting to stress estimates following Large and Pond (1981). Air-sea bulk heat and momentum fluxes are calculated as in Fairall et al. (1996). Both stress and flux estimates were performed in MATLAB using the air-sea toolbox of Pawlowicz et al. (2001).

Auxiliary data at R2 also included 5 min–averaged water temperature (T) measurements obtained throughout the water column from internally recording Onset Hobo T sensors (Onset, Bourne, MA) arranged on a T-chain with 1 m interval. Individual records were adjusted to eliminate mean temperature inversions over sequential T-chain deployments (each of ∼6-month duration). Surface and bottom conductivity-temperature (CT) packages (Seabird, Bellevue, WA) sampled continuously and recorded averaged values over 6 min intervals.

Measurements from a ParoScientific (Redmond, WA) pressure gauge mounted on the R2 tower at 6 m below mean sea level are corrected for pressure attenuation with depth using linear wave theory (eliminating frequencies of 0.25 Hz and higher to avoid noise amplification; Bishop and Donelan 1987) and then integrals of spectra over 6 min intervals are used to estimate significant wave height.

3. Observational results characteristic of LSs

One of several large wind- and wave-coincident, full water column backscatter events observed during 2007–2008 at R2 is shown in Figure 2. As wind speed and significant wave height increased, high backscatter signals along the VADCP vertical fifth beam developed first in the upper water column, likely because of bubble clouds from breaking waves (Fig. 2a). Water column stratification rather abruptly disappeared late on 16 September (Fig. 2c), coincident with increased backscatter signal near the bottom. By early morning of 17 September, the entire water column was engulfed in backscatter. Strong vertical velocities were detected in the VADCP fifth beam (Fig. 2b), commencing about the time when full water column high backscatter began and continuing through and somewhat past the end of the high wind/wave event (Fig. 2e and f). This is reminiscent of the event at LEO that Gargett et al. (2004) showed was attributable to full-depth Langmuir circulations (i.e., LSs).

In the following, we diagnose the existence of LSs during the high wind and wave event of Figure 2, using various methods developed for the LEO VADCP deployment (Gargett and Wells 2007; Tejada-Martínez and Grosch 2007; Gargett and Grosch 2014; Gargett, Savidge, and Wells 2014). We refer the reader to these references for details beyond those provided here. The "units" analyzed are typically the 2 h records of each session's high-frequency data. Similar trial analyses of 1 h segments or of the middle 2 h of two concatenated sequential 2 h blocks result in similar outcomes as described in this section.

a. Fluctuating three-dimensional velocity fields in wind coordinates

Stationary instruments measure some combination of temporal and spatial variability in the water column as conditions change and/or as spatial circulation structures drift past the mooring position. Inspection of the auxiliary data was first used to select records for which the wind was relatively constant in direction and magnitude. The 2 h intervals also satisfy a requirement for slowly varying tide over their duration. For such records, the variation recorded by the stationary VADCP can be interpreted as predominantly spatial in origin. Horizontal velocities are presented in wind coordinates, with the x-axis oriented downwind as determined from the 2 h mean for each wind record. Crosswind velocities are positive to the left, looking downwind.

Three-dimensional wind-coordinate VADCP velocity data from two sequential records collected on 19 September are shown in Figure 3. Primed variables are calculated from the 10 s data and have had the 2 h mean and linear least squares trend removed from each bin. For visualization purposes, data in this figure have been further smoothed in time with
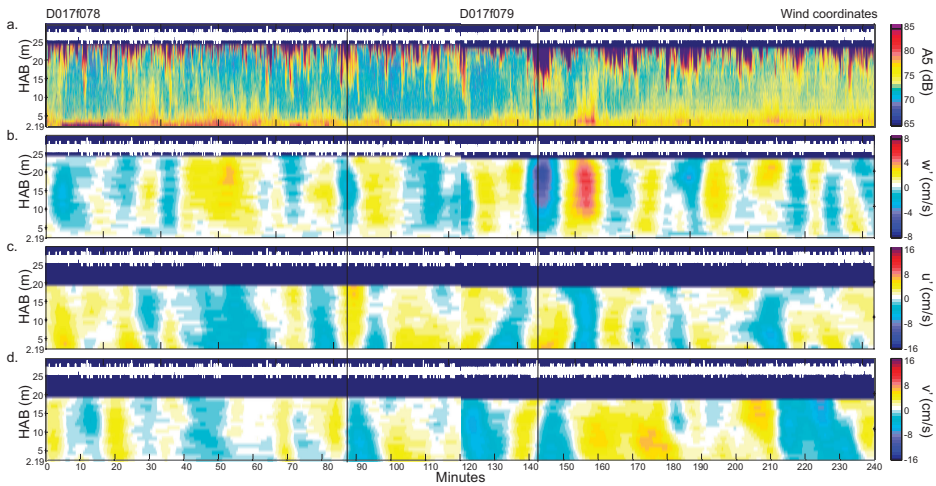
Figure 3. Backscatter and velocities from session 17, records 78 and 79, plotted as functions of time and height above bottom, with surface location (0.95 m resolution) determined in fifth beam backscatter: (a) fifth beam backscatter; (b) fifth beam vertical velocity, w'; (c) horizontal wind-aligned velocity, u' (positive downwind); and (d) wind-normal velocity, v' (positive to left of downwind). Backscatter has not been filtered: velocities were first filtered to remove waves and then further smoothed for plotting (as described in the text). Vertical lines highlight two examples of in-phase near-surface backscatter, downwelling vertical velocities, and downwind horizontal velocities, with near-bottom crosswind velocities ~90° out of phase, structure diagnostic of Langmuir supercells. Panels are plotted as a function of height above bottom (HAB) in m.

a 10 min Hanning window, though all diagnostic analyses use 10 s data. Periods of large downward vertical velocities (downwellings) generally correspond with large downwind velocities and high nearsurface backscatter from the vertical beam. Conversely, large upward vertical velocities (upwellings) correspond with large upwind velocities and high backscatter near bottom. Near-bottom crosswind velocity tends to change sign below downwellings and upwellings, with phase determined by the direction of V, the mean crosswind flow with which turbulent features drift past the VADCP. In this case, $V > 0$ (to the left of the downwind direction), so positive v' preceding a downwelling switches to negative v' following it.

The features seen in Figure 3 are consistent with the existence of counterrotating cell pairs characteristic of Langmuir circulations that fill the water column. However, the cell structures observed at R2 appear generally less well organized than those at LEO. For example, in comparison with figure 6 of Gargett and Wells (2007), the structures at R2 in Figure 3 are less uniform in size, the crosswind convergence and divergence near bottom is less well aligned with upwelling and downwelling centers, and bottom intensification of downwind velocities is less apparent.
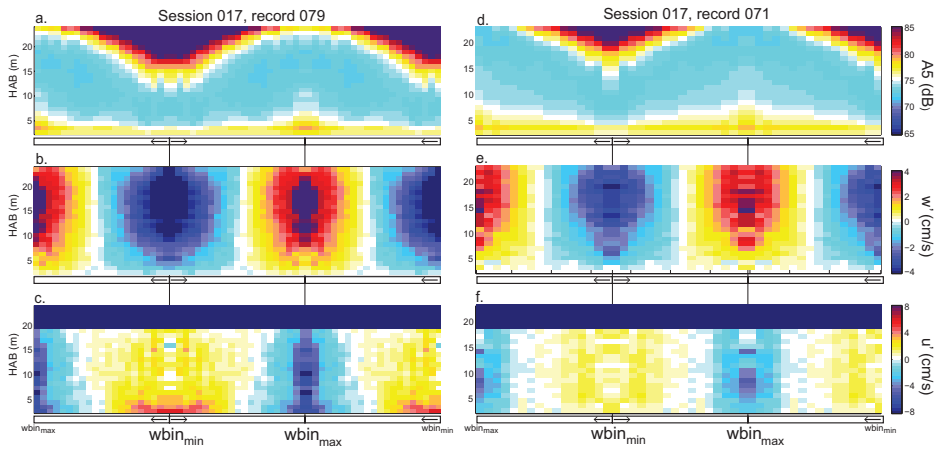
Figure 4. Conditionally averaged backscatter and velocity fields from records in session 17 with strong (79; a, b, c) and weak (71; d, e, f) Langmuir supercell characteristics. Data are binned by vertically averaged vertical velocity, $\overline{w'}$, ranging from minimum to maximum $\overline{w'}$ in 0.5 cm s^{-1} intervals. Results are mirrored along the x-axis to mimic the quasi-sinusoidal nature of the vertical velocity time series. (a and d) Fifth beam backscatter. (b and e) Fifth beam vertical velocity, w'. (c and f) Wind-aligned horizontal velocity, u', positive downwind. Panels are plotted as a function of height above bottom (HAB) in m.

To better visualize the ordered relationships that the Langmuir cell structure imposes on the three-dimensional fluctuation velocities, data have been conditionally averaged relative to vertically averaged vertical velocity, $\overline{w'}$. Time series of w', u', and backscatter amplitude profiles were sorted into bins corresponding to values of $\overline{w'}$ ranging from $(\overline{w'})_{min} = -4$ cm s^{-1} to $(\overline{w'})_{max} = +4$ cm s^{-1} in 0.5 cm s^{-1} increments and then averaging the profile data in each bin. These conditional averages are plotted as a function of $\overline{w'}$, with bins running from $(\overline{w'})_{max}$ to $(\overline{w'})_{min}$; $(\overline{w'})_{min}$ to $(\overline{w'})_{max}$; and $(\overline{w'})_{max}$ to $(\overline{w'})_{min}$ (i.e., mirrored along the x-axis to mimic the quasiperiodic nature of the vertical velocity time series). Figure 4 shows results from two records during the September event: records 79 and 71 are respectively from periods of relatively more or less well-defined structures (see further discussion in Section 3d). Correlations among w', u' and backscatter expected for Langmuir circulations are clearly shown for record 79: strong negative/positive w' in phase with downwind/upwind horizontal velocity u' and surface/bottom-intensified increased backscatter, consistent with downwelled bubble clouds/upwelled bottom sediments (Fig. 4a–c). Both upwind and downwind maxima are slightly bottom intensified. Although features are weaker in the conditional averages of record 71 (Fig. 4d–f) the characteristics detailed previously are still present.

Although the structures expected of Langmuir circulations in the u' and w' velocity components are horizontally symmetric in the crosswind direction about maximum or minimum
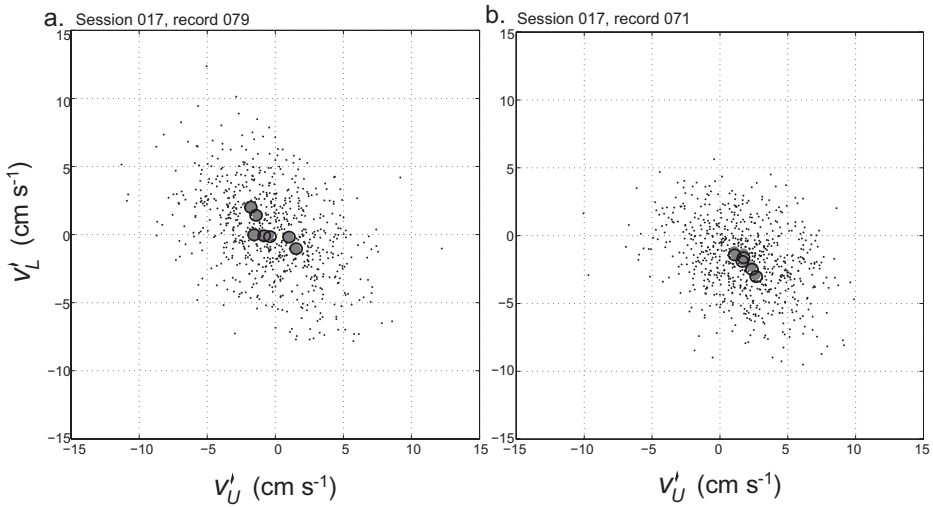
Figure 5. Scatter plot of upper (v'_U) and lower (v'_L) water column crosswind velocities from the records of Figure 4. Data have had vertical average velocities subtracted. The elliptical shape and orientation of both 10 s data (small black points) and 15 min averages (large gray dots) indicate opposing crosswind flow in the upper and lower water columns, consistent with expected circulation in Langmuir cells.

$\overline{w'}$, the expected crosswind component v' of Langmuir cells is 90° out of phase with $\overline{w'}$, so conditional averaging of v' by $\overline{w'}$ is not appropriate. Furthermore, unlike the downwind and vertical components, the sign of the crosswind component is expected to reverse with depth in Langmuir cells, with maximum magnitudes expected in the near-surface and near-bottom boundary layers. Both such layers are poorly sampled by this deployment because of side-lobe pickup through 15% of the upper water column with the 30° slant beams and the absence of very near-bottom measurements, as the first bin is centered 2.1 mab. Nonetheless, to investigate whether vertical shear in the crosswind component consistent with LSs exists, upper and lower crosswind velocities are plotted against one another in Figure 5 for the same 2 h periods of Figure 4, using VADCP bins 3 (4 mab) and 16 (16.3 mab), with water column average velocity removed at each time point. The elliptical shape and orientation of both the 10 s data (small black points) and 15 min averages (large gray dots) indicate opposing crosswind flow in the upper and lower water columns, consistent with expected circulation in Langmuir cells. Although many processes in the coastal ocean result in vertical shear in the approximately cross-shelf oriented component the shear depicted in Figure 5 changes sign at relatively high frequency, evident in the fact that the 10 s data cover a much broader range of velocities than 15 min averages. Alternating sign at periods shorter than 15 min is consistent with a sequence of LSs drifting past, rather than some more slowly varying process.

b. Profiles of normal and shear stresses

Turbulent statistics were calculated by bin for each 2 h block, providing vertical profiles of mean velocity components, normal stresses (variances) $<u'u'>$, $<v'v'>$, and $<w'w'>$ and shear stresses $<-v'w'>$, $<-u'w'>$, and $<-u'v'>$. Brackets indicate the temporal average.

Profiles of normal and shear stresses from records during high winds and waves at R2 show characteristic features of LSs. Specifically, normal stress profiles frequently exhibit large bottom-intensified downwind component $<u'u'>$ (Fig. 6a). This near-bottom maximum, or "nose," is absent in measurements or models of deep-ocean Langmuir cells but is an important diagnostic in the bottom-bounded cases examined by the combined observational and large-eddy simulation (LES) study at LEO (Gargett and Wells 2007, Tejada-Martínez and Grosch 2007). Other stress profile features that were diagnostic at LEO and also evident at R2 include the following: near-bottom $<v'v'>$ values that are smaller than $<u'u'>$, growing to values similar to $<u'u'>$ in the middle to upper water column; vertical normal stress $<w'w'>$ (Fig. 6b) small near the bottom, growing to values near those of $<u'u'>$ and $<v'v'>$ in the middle to upper water column; large positive values of $<-u'w'>$ that are relatively constant with depth; and values of $<-v'w'>$ near zero throughout the water column (Fig. 6c). At R2 as at LEO, the third shear stress component $<-u'v'>$ (not shown) can be relatively large and variable with depth in any given 2 h estimate but tends to zero at all depths when averaged over several 2 h records.

Profiles of higher-order statistical quantities (Pope 2000) calculated from three-dimensional velocity data for each bin of the VADCP data are depicted in the so-called Lumley triangle (Fig. 6d). Shapes of these depth-dependent invariant (to rotation) traces can distinguish between turbulence driven solely by shear stress or by the Langmuir vortex force (Gargett and Wells 2007; Tejada-Martínez and Grosch 2007). Strong Langmuir cells at LEO produced a highly distinctive trace: the cell nearest the bottom (0.8 mab) starts on the upper boundary of the triangle, then curves in a characteristic "C" shape toward the right boundary over the bottom third of the water column and lies along the left boundary through interior bins, before moving to the left boundary for data from upper water column bins (below the upper 15% corrupted by side-lobe pickup). Unfortunately, at R2 the very near-bottom velocity measurements necessary to define the "C" shape are missing, as the bin nearest bottom was centered at 2.1 mab. Nonetheless, the well-sampled interior shows a trace that generally lies along the left boundary of the Lumley "triangle," with a depth-limited excursion toward the right boundary. This result is consistent with those for LSs at LEO. They are inconsistent with turbulence generated by stressdriven flows (Tejada-Martínez and Grosch 2007) or convective turbulence (Gargett and Grosch 2014).

Figure 7 shows similar profiles for the record with weakened structures seen in Figure 4b. The near-bottom maximum in $<u'u'>$ is reduced, as are the magnitudes of the normal and shear stresses. However, the conditionally averaged structure (Fig. 4b) is still that of a full-depth Langmuir circulation, and the Lumley trace still lies along the left-hand boundary of the Lumley triangle, evidence that LS structures are present throughout the event of Figure 2.
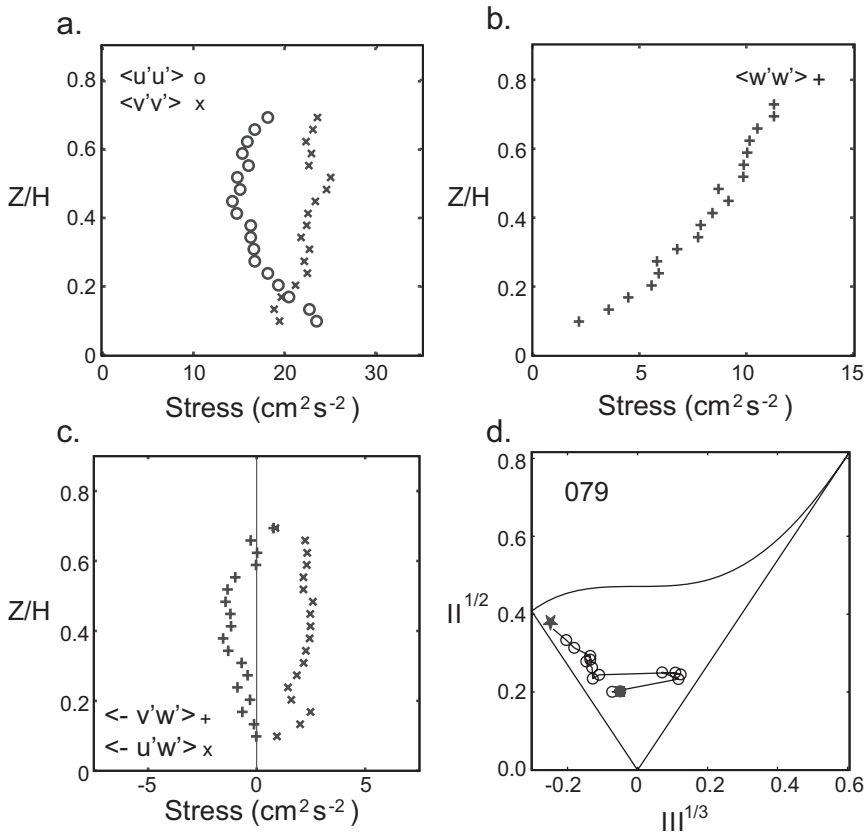
Figure 6. Vertical profiles of statistical properties closely resembling those found to be diagnostic of Langmuir supercells at the Long-Term Ecosystem Observatory, calculated from record 79 of session 17 vertical beam acoustic Doppler current profiler (VADCP) 10 s detrended velocity data, bins 1 through top slant bin uncontaminated by side-lobe interference. (a) Horizontal wind-aligned $<u'u'>$ (symbol "o") and wind-normal $<v'v'>$ (symbol "x") variances. (b) Vertical velocity variance. (c) Wind-aligned and wind-normal shear stresses, respectively, $<-u'w'>$ (symbol "x") and $<-v'w'>$ (symbol "+"). (d) Trace in the Lumley triangle, from VADCP bin 1 near bottom (star) through top slant bin uncontaminated by side-lobe interference (solid circle).

c. Inference of wind elongate structure

Langmuir cells are expected to be elongated in the along-wind direction. To investigate, we use a wavelet transform method (Gargett and Wells 2007) to analyze fifth beam vertical velocity (Fig. 8a) from bin 4 (4.9 mab) for the event of Figure 2, focusing on 16–20 September when wind speed, wind direction, significant wave height, and low-frequency mean current speed and direction were all fairly constant. It is then reasonably assumed that during this period the dominant wind-generated surface waves are wind aligned. The
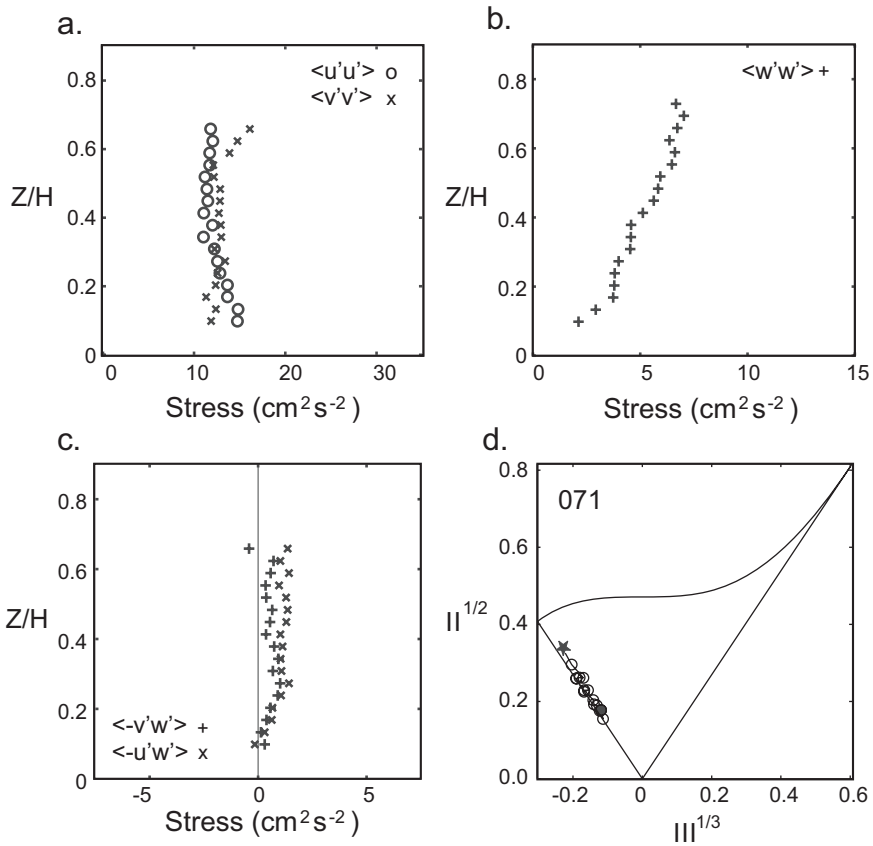
Figure 7. Vertical profiles of statistical properties closely resembling those found to be diagnostic of Langmuir supercells at the Long-Term Ecosystem Observatory, calculated from record 71 of session 17 vertical beam acoustic Doppler current profiler (VADCP) 10 s detrended velocity data, bins 1 through top slant bin uncontaminated by side-lobe interference. (a) Horizontal wind-aligned $<u'u'>$ (symbol "o") and wind-normal $<v'v'>$ (symbol "x") variances. (b) Vertical velocity variance. (c) Wind-aligned and wind-normal shear stresses, respectively, $<-u'w'>$ (symbol "x") and $<-v'w'>$ (symbol "+"). (d) Trace in the Lumley triangle, from VADCP bin 1 near bottom (star) through top slant bin uncontaminated by side-lobe interference (solid circle).

apparent period of turbulent fluctuations measured at the VADCP should vary with the strength of (tidally varying) flow advecting turbulent features past the VADCP. Strong temporal variability in the dominant apparent period is evident in the wavelet power spectrum shown in both Figure 8(b) and (c). This is consistent with strong variation in the magnitude of the advecting tidal velocities, assuming cell size is relatively constant.

If the features are elongated approximately along-wind, the apparent period will be determined by only the crosswind component of the flow, whereas horizontally isotropic
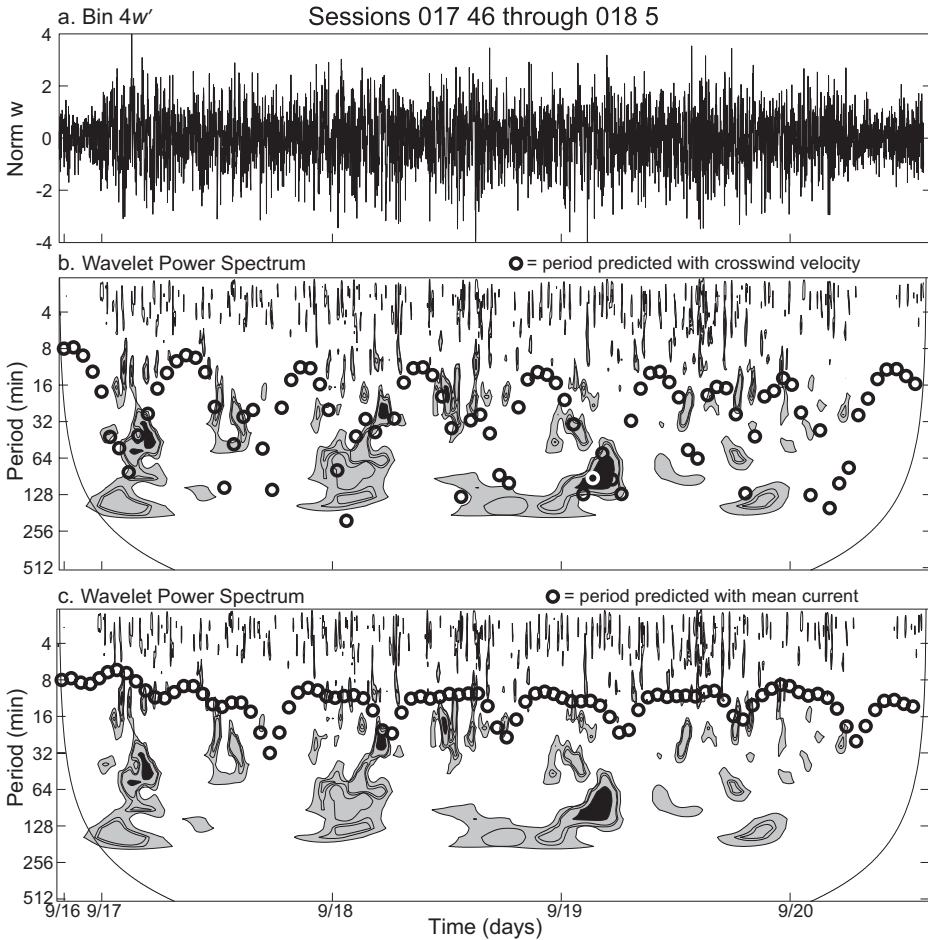
Figure 8. Wavelet analysis of vertical velocity w' (bin 4, 4.9 meters above bottom) from the September 2007 Langmuir supercell event. (a) The w' time series. (b) Wavelet analysis with period predicted hourly using the crosswind component of total (mean plus tidal) flow. (c) Wavelet analysis with period predicted using total flow magnitude.

features would be carried past the VADCP by the total flow regardless of direction. Using the dominant period at the start of the analysis period plus the low-frequency (mean plus tidal) velocity measured by the VADCP at that time, we first estimate a horizontal crosswind size of ∼90 m for the features assumed to be drifting past the VADCP. Further assuming that this scale remains constant, measured horizontal velocities over successive hourly intervals are used to predict the periods at which features of this size would appear at the VADCP. These values are plotted as black circles for two cases, in which periods are predicted with only the crosswind flow component (Fig. 8b: wind-elongate assumption) or the total flow speed
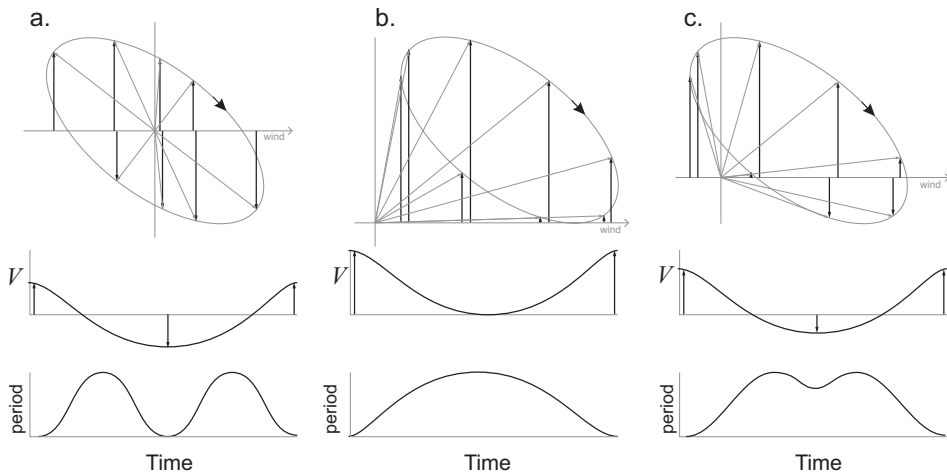
Figure 9. Schematic cross-shelf-oriented M2 tidal ellipses in wind coordinates, assuming a wind direction rotated somewhat shoreward of alongshore. The upper panel of each set depicts total (gray vectors) and crosswind (black vectors) velocities at various times during the tidal cycle. Tidal velocities on the Georgia shelf move clockwise in time about the ellipse, as shown. Schematic temporal evolution of the crosswind velocity is plotted in the middle panels, whereas the lower panels show the resulting period of wind-aligned, constant horizontal-scale Langmuir supercells advected past the vertical beam acoustic Doppler current profiler. (a) A situation where only tidal velocities are present. (b) An along-shelf mean velocity (normal to the semimajor axis of the tidal ellipse) is large enough that total (tide plus mean) crosswind velocity never reverses. (c) A situation with along-shelf mean flow somewhat weaker than panel (b).

(Fig. 8c: isotropic assumption). The wind-elongate assumption is clearly more successful at predicting the magnitudes and time variability of apparent periods observed in the wavelet power spectrum, as well as consistent with the associated Lumley triangle traces which indicate anisotropic structures.

Although we thus infer that the large-eddy structures are wind elongate, the apparent period is not what would initially be expected from advection by the predominantly semi-diurnal tidal velocities on the Georgia shelf. M2 tidal velocity magnitudes peak on both flood and ebb phases, every 6.21 h, so the dominant time between maxima in apparent periods would be expected to be 6.21 h, as shown schematically in Figure 9(a). Instead, the wavelet analysis shows an approximately semidiurnal period (i.e., twice that expected from a semidiurnal tide). However, the turbulent structures are not advected exclusively by the tides. In this laterally bounded coastal domain, storm winds from the northeast drive shoreward Ekman transport which sets up an offshore pressure gradient and shore-parallel geostrophic mean flow. Addition of shore-parallel mean flow to a shore-normal tidal ellipse offsets the total (tidal ellipse plus geostrophic mean) from the origin. When the wind is at an angle to the shore-parallel flow, that offset changes the apparent period at which

wind-aligned features are advected past the VADCP by the crosswind component of the total flow. For mean crosswind current magnitude as large or larger than the tide, period maxima at twice the M2 tidal frequency are eliminated (Fig. 9b), as crosswind velocities never actually reverse. Geostrophic along-shelf velocity somewhat smaller than the maximum tidal velocities leads to unequal crosswind velocities, and hence unequal apparent periods between maximum flood and ebb phases of the tide (Fig. 9c).

A hodograph of measured low-frequency (mean plus tidal) midwater velocities in wind coordinates during the LS event of Figure 2, shown in Figure 10(a), has features of the schematics in both Figure 9(b) and (c). The along-wind component of the mean flow is larger than that of the tide: as in Figure 9(b), the total along-wind flow never reverses. The crosswind mean flow is (only slightly) smaller than that of the tide, resulting in the asymmetric total crosswind flow of Figure 9(c) and hence a dominant variation in apparent period of ∼12.41 h.

d. Time variability of LSs

Although the features described previously confirm the existence of LSs at 26 m depth during the high wind and wave event examined and in other similar events, the observed velocity structures are clearly less organized at R2 than at LEO (Fig. 3; Section 3c). In addition the R2 observations, unlike those at LEO, show modulation of several diagnostic features with time, with major periodicity of ∼12 h. Temporal variability of both unfiltered backscatter strength and filtered 10 s vertical velocity is visually apparent at an ∼12 h period (Fig. 2). That the variability in the 10 s data is real, not an artifact of filtering is illustrated by its appearance in the unfiltered backscatter data. The Appendix further demonstrates both a spectral gap between waves and lower-frequency variability and the absence of tidal variation at frequencies within that gap. As discussed in Section 3c, given wind-aligned Langmuir structures, the observed modulation period of ∼12 h is that associated with the superposition of approximately shore-normal tide plus shorealigned geostrophic current during LS events.

Two metrics of temporal variability are derived from features deemed diagnostic of LSs. The first is $\overline{\langle w'^2 \rangle}$, vertical velocity variance of the fifth beam 10 s data, time-averaged over each 2 h record (bracket) and then depth averaged (overbar) from bin 3 through the last subsurface bin. Nonstorm values of this metric are ∼(0.2–0.3) $\times 10^3$ m^2 s^{-2} before and after the September 2007 LS. During the event, values range from ∼(0.4–0.8) $\times 10^{-3}$ m^2 s^{-2}, with peaks at roughly 12 h intervals (Fig. 11b). This is somewhat higher than found at LEO.

The second metric is defined as $\mathcal{N} = <u'u'>/<v'v'>$ where $<u'u'>$ from a near-bottom bin is normalized by $<v'v'>$ from the same bin. This ratio highlights those records where the near-bottom structure most clearly exhibits the LS characteristic of the horizontal normal stresses shown in Figure 6(a)—namely a nose in $<u'u'>$, with $<v'v'>$ less than $<u'u'>$, hence $\mathcal{N} > 1$. Note that data from the R2 deployment is not ideal for calculation of $\mathcal{N}$ because the VADCP did not sample the lower boundary layer well. Moreover, the bottom two slant beam bins occasionally showed interference from vertical beam side lobes
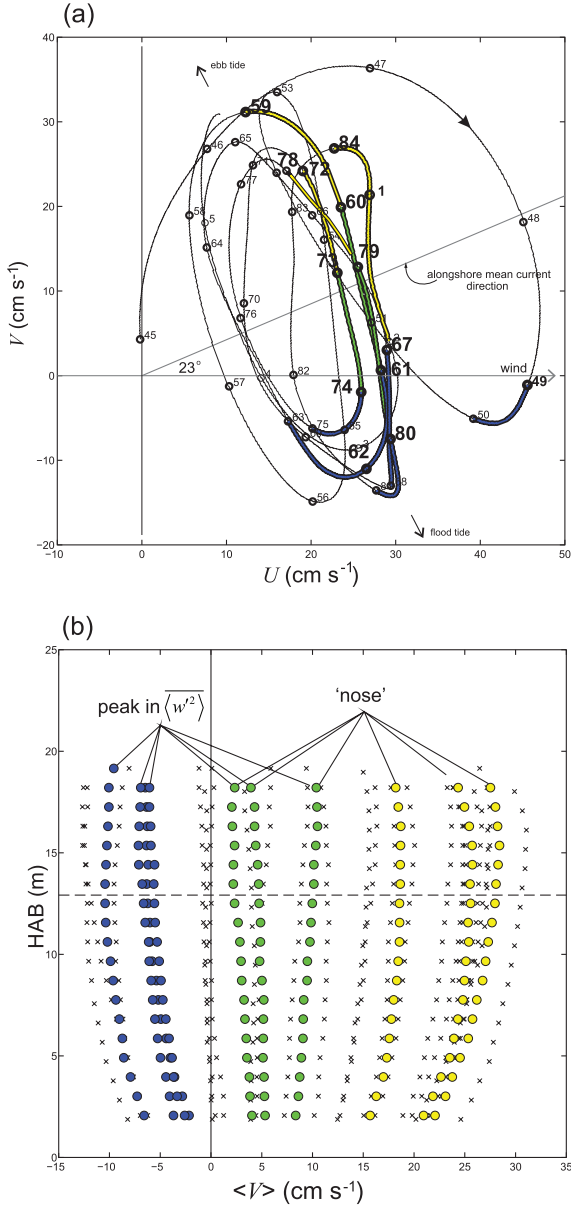
Figure 10. Horizontal velocities during the September 2007 event shown in Figures 2–7. (a) Hodograph of 10 s velocities from bin 11 (11.6 meters above bottom), shown in wind coordinates. The x-axis is oriented in the direction toward which the wind is blowing (228° clockwise from north). The time-mean current direction, ∼23° to the left of the wind, is approximately shore parallel perpendicular to the cross-shelf–oriented tidal ellipse. The start of each record is marked with a small circle and the record number (45–84 from session 17, followed by records 1–5 from session 18). (b) Vertical profiles of crosswind velocities for session 17, records 50–84. Colors in both panels represent records when a nose diagnostic (yellow) or a $\overline{\langle w'^2 \rangle}$ diagnostic (blue), as defined in Section 3d, is fulfilled. Green symbols are records in which both diagnostics are fulfilled simultaneously, indicating particularly strong and well-organized Langmuir supercells.
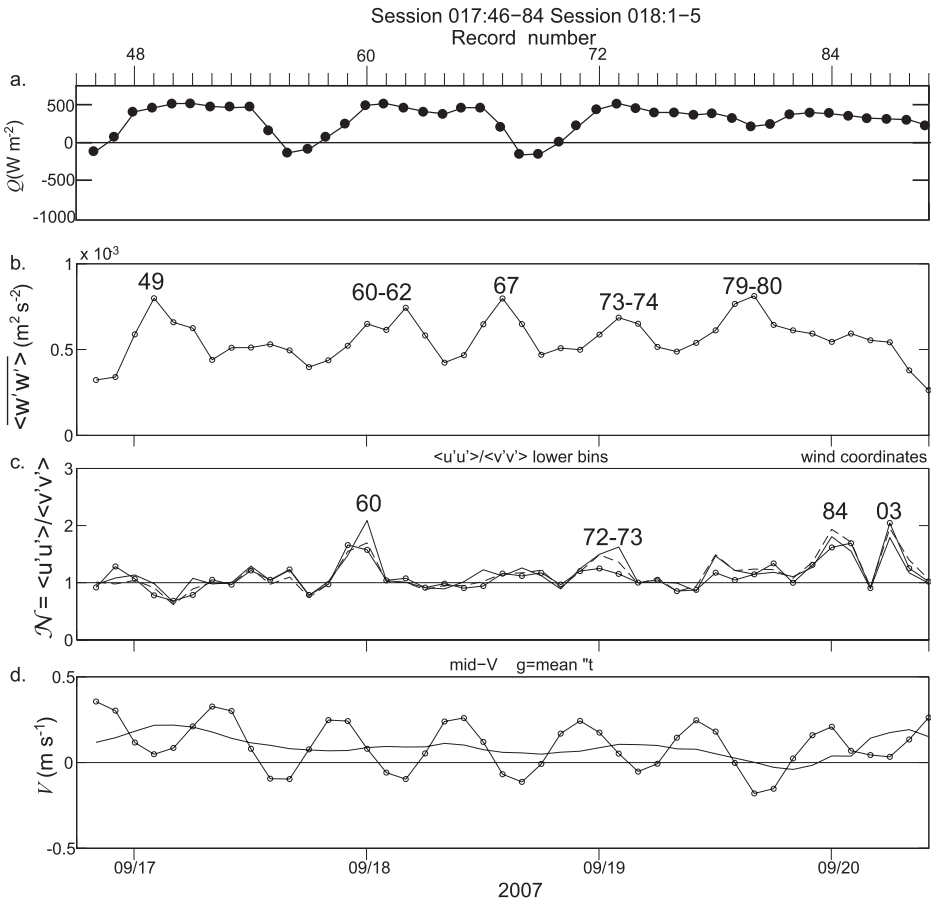
Figure 11. Time series of 2 h average quantities during the Langmuir supercell event of Figure 2: session 17, records 46–84 and session 18, records 1–5. (a) Surface heat flux, positive out of the ocean. (b) Depth-averaged vertical velocity variance $\overline{\langle w'^2 \rangle}$. (c) Nose diagnostic $\mathcal{N} = \overline{\langle u'u' \rangle}/\overline{\langle v'v' \rangle}$ for bins 1–3 (bin 1, line with circles; bin 2, dashed line; bin 3, solid line). (d) Middepth horizontal crosswind velocity, V (line with circles represents tide plus slowly varying mean; solid line represents mean only). Wind direction shifted suddenly at record 18.03, the third data point after record 17.84, the last record of session 17. Records discussed in the text are marked with record numbers in panels (b) and (c).

(although no such records are included in Figs. 3–5). Bin 3, which is the most uniformly reliable, is farthest from the boundary (3.9 mab), where $\langle v'v' \rangle$ may be already approaching $\langle u'u' \rangle$ in magnitude. Despite these caveats, the time series of $\mathcal{N}$ (Fig. 11c) reveals some peaks with $\mathcal{N} > 1$ in all three near-bottom bins, with the largest occurring at $\sim$24 h intervals (records 17.60, 17.72–73, and 17.84). The peak in 18.03 is discounted because the wind

had begun to shift direction at the end of the storm, calling the assumption of wind and wave alignment into question. Inspection of vertical profiles of $<u'u'>$ confirm that these are indeed records with well-developed near-bottom noses.

In the following discussion of time dependence, "tide" or "tidal" will be used to refer to the periodicity produced by the superposition of tidal flow with the roughly shorealigned geostrophic storm response. The phase of tide when each diagnostic peaks is shown on the hodograph of Figure 10(a). In both Figures 10(a) and (b), records with $\langle w'^2 \rangle$ peaks are marked in blue, records with $\mathcal{N} > 1$ appear in yellow, and records with both features are green. Figure 10(b) illustrates both magnitude and shear of the crosswind velocities at times when either or both of the diagnostics show peaks.

Peaks in the nose diagnostic generally occur earlier in the tidal cycle than the distinct maxima in $\langle w'^2 \rangle$ (Fig. 10 a and b). As a result of this difference, records characterized by both a peak in $\langle w'^2 \rangle$ and a well-defined nose in $<u'^2>$ lie roughly midway between the directions of the time-mean current and that of the wind. This result is suggestive of the analysis by Gnanadesikan and Weller (1995) of a simplified case where surface directions of linear Eulerian shear and linearized Stokes drift shear differ by angle θ: they found that maximum growth rate of Langmuir circulations occurs at θ/2 if both shears are equal in magnitude and closer to the larger shear when they are unequal.

The wavelet analysis of Figure 7 suggests that there is also a weak diurnal signal in the R2 observations: note the appearance of longer period (64–128 min) components on a diurnal timescale, perhaps indicative of scale modulation by the addition of convection during the nighttime periods of surface heat loss seen in Figure 11(a). However, the $\langle w'^2 \rangle$ diagnostic does not show clear diurnal variability—although some peaks in $\langle w'^2 \rangle$ are coincident with nighttime periods when $Q > 0$ (Fig. 11a), others are not.

e. Forcing

We note finally that during events at tower R2 for which in-water characteristics indicate LSs, forcing is consistent with that seen during LSs at LEO. In particular, the water column is unstratified, and regime diagrams, plotted as defined in either Li et al. (2005) or Gargett and Grosch (2014), indicate values near or below thresholds (Li et al. 2005; Gargett, Savidge, and Wells 2014) that imply dominance by the so-called vortex forcing of Craik and Leibovich (1976) over buoyancy and shear stress. Furthermore, the coincident wave field at R2 is intermediate in character when LSs exist, and a near-linear relationship between near-bottom and near-surface turbulent growth rates is established. Both features were present whenever LSs were observed at LEO (Gargett, Savidge, and Wells 2014) and both indicate that when waves "feel the bottom" (i.e., transition from deep to intermediate character) vortex forcing extends throughout the water column. Further exploration of such metrics to allow the determination of LS likelihood in different shelf locations in the absence of VADCP data will be addressed in a subsequent article (D. K. Savidge and A. E. Gargett, unpublished).

4. Discussion

The previous section has documented overall weaker (i.e., less highly structured) full-depth Langmuir cells at R2 than at LEO, with temporal modulation in both strength and organization at certain phases of the tide, variability not seen at LEO. Nonetheless, full-depth cells appear to be present throughout the period of near-constant wind/wave forcing, with elevated $\overline{\langle w'^2 \rangle}$ and backscatter through all phases of the tide and wavelet analysis indicating wind-aligned features advecting past the VADCP throughout the event. Even the "disrupted" structures with somewhat lower u' and w' magnitudes and a reduction of the bottom intensification of u' exhibit LS-consistent features in conditional averages (Figs. 4 and 5), as well as invariant traces lying on the left-hand side of the Lumley triangle (Fig. 7).

The overall less organized structure and temporal modulation in the LSs observed at R2 illuminate potential constraints on the development and persistence of LSs in the coastal ocean. In the following, mechanisms are identified that might contribute to contrasts between the R2 LSs and the stronger more stable features observed at LEO. For clarity, these mechanisms are presented as contributing to either reduced organization of LSs or the modulation of their diagnostic features on short timescales. However, these two categories are likely interrelated: generally weaker structures may be more susceptible to disruption by variable conditions while, conversely, temporally modulated forcing may integrate over time to overall weaker structures. Because of the absence of detailed velocity structure in either surface or bottom boundary layers in the R2 measurements, these discussions are largely qualitative. The purpose is to consider which processes are likely contributing, for the circumstances peculiar to the SAB. This will provide direction for future observational efforts in different depth and forcing range settings, and additional LES diagnostic modeling, to isolate and examine subsets of interacting disruptive agents.

a. Less organized structure

i. Marginal hydrodynamic stability. Although there are no theoretical results that predict the horizontal cell size of Langmuir cells, the LS horizontal scales are approximately the same at the LEO and R2 sites, ~90 m, as estimated by wavelet analyses. We have no explanation for this curious result but note that dominant surface wave wavelengths at the two sites are similar. Thus, because water depths differ at the two locations, the width-to-depth ratio of full-depth cells at R2 is only ~3, in contrast to the value of 5–6 typical for LEO. According to a theoretical criterion derived by Rosenhead (1929), and adapted by Thorpe (1992) for the case of Langmuir circulations, a width-to-depth ratio of 3 implies only marginal stability of the paired vortices characteristic of Langmuir circulations. The weakness of Langmuir cells at R2 may thus be primarily attributable to basic hydrodynamic instability, rather than any of the other processes described subsequently. However, the results of Thorpe (1992) require several simplifying assumptions that may not directly apply to R2—in particular, that the vortex forcing has ceased for the conditions examined in the stability analysis. Further, depending on whether the disturbance applied is two or three dimensional, the

stability criterion can change quite drastically (see Thorpe's figs. 7–9). Further examination by LES for the R2 parameter space cases will be necessary to confirm the importance of instability.

ii. Weakened near-bottom forcing. The vertical extent of Langmuir cells is also not predicted theoretically, for either deep-ocean or bottom-bounded cases. However, vertical extent in the coastal ocean, in the absence of stratification, does depend on the character/magnitude of vortex forcing. Tejada-Martínez and Grosch (2007) carried out a limited exploration of the effect of the ratio of dominant surface wave wavelength λ to depth H on LSs, using a value of turbulent Langmuir number $La_t \equiv (u_*/u_{S0})^{1/2} = 0.7$, characteristic of wind/wave storm forcing levels at both LEO and R2. (See Gargett and Grosch [2014] and Gargett, Savidge, and Wells [2014] for estimation details of the surface stress velocity u_* and surface Stokes velocity u_{S0} from these data sets.) For fixed La_t, they found that smaller λ/H resulted in weaker imprint of Langmuir cells on the structure of the turbulence in the lower part of the water column. Furthermore, Kulkulka et al. (2011) found that disruption of Langmuir structure was diminished under conditions of stronger near-surface wave forcing (lower La_t), for crosswind tidal velocities sufficient to disrupt such structure at higher (but still vortex-force dominant) La_t. The weaker LSs at R2 are consistent with such results, with both diminished λ/H, relative to LEO, and near threshold vortex-forcing dominance (Section 3e).

iii. Misalignment between directions of current and wind/waves. Because of differences in dominant storm wind direction relative to the strike of coastlines, the mean (wind-forced geostrophic) alongshore flow during storms lies to the left of the wind at both LEO and R2. Assuming wind and waves are aligned, generation of Langmuir circulation is typically attributed to near-surface vertical vorticity pairs (produced by crosswind perturbations in the stress-driven Eulerian mean flow) being rotated to horizontal by the vertical shear of wind and wave-aligned Stokes drift velocities (see Fig. 3 of Leibovich 1983). Misalignment between the near-surface directions of mean (parallel to the coast) and Stokes (wind-aligned) flows can certainly reduce the efficiency of this generation process, as documented in the steady-state calculations of Gnanadesikan and Weller (1995). With misalignment evident at both LEO, where strong LSs existed, and at R2, where the LSs are weaker, misalignment may not be the primary cause of the differences in LSs between the sites. However, one significant difference between the sites is that the background mean at R2 is modulated by a very large tide, so that the misalignment between the wind and the mean plus tide varies from nearly 60° left of the wind/wave direction at maximum ebb to 30° to the right of the wind/wave direction at maximum flood (Fig. 10a), subtending a nearly 90° angle. By contrast, the LEO misalignment subtends only 30° total, all left of the wind. The VADCP observations at neither location provide near-surface horizontal velocity or near-surface shear. Such observations are necessary to evaluate the dependence of generation efficiency on misaligned shears.

b. Time dependence

i. Enhanced bottom boundary shear associated with tides. Maximum tidal flow of $O(0.3$ m s$^{-1})$ at R2 is considerably stronger than $O(0.1$ m s$^{-1})$ tidal flows at LEO, raising the possibility that additional bottom boundary layer shear (and associated turbulence) driven by pressure gradients and oriented over a wide range of angles to the wind interacts with LSs at R2 to contribute to the time-variability seen there. Numerical modeling studies are not in agreement over the effects of pressure gradient–driven mean currents on Langmuir circulation in a bottom-bounded regime. Dartus et al. (2000) suggest that collinear flow associated with a pressure gradient in the direction of the wind enhances full-depth Langmuir cells, while Martinat, Grosch, and Tejada-Martínez (2011) report structures that are disrupted, particularly in the bottom half of the water column, by collinear flow but resistant to cross flow. Because the former study is scaled using a "turbulent eddy viscosity," whereas the latter is run with scales typical of LEO measurements, neither is directly applicable to our observations. However, the observations do exhibit distinct phasing relative to the magnitudes of collinear and normal tide plus mean flows.

If stronger bottom boundary layer shear and turbulence acted to enhance LSs, as suggested by Dartus et al. (2000), it would be expected that LS structures would be most distinct during periods when tide plus mean flow magnitude was maximal in the direction of the wind (i.e., on the region of the hodograph shown in Figure 10(a) that is farthest from the origin). The observations indeed demonstrate this phasing. Records with distinct near-bottom noses (yellow and green in Fig. 10a and b) are found near and after maximum ebb, when tide plus mean magnitude is large. Records with elevated $\langle w'^2 \rangle$ (green and blue in Fig. 10a and b) are found before and during maximum flood, when tide plus mean flow magnitude is maximal. The hodograph also shows that records exhibiting noses and/or elevated $\langle w'^2 \rangle$ encompass a range of small to large crosswind component, suggesting, as did Martinat, Grosch, and Tejada-Martínez (2011), that the structures are not strongly influenced by crosswind pressure gradient–driven flow. Understanding of the effects of collinear and cross flows associated with pressure gradient–driven flows like that of the tides would be advanced by observations closer to the bottom than those at R2, and by LES carried out with scales relevant to the R2 study site.

ii. Middepth crosswind current shear associated with tides. Two possible mechanisms whereby crosswind tidal currents outside the bottom boundary layer might disrupt wind-aligned Langmuir cells in a tidally varying flow were proposed by Kukulka et al. (2011). Both mechanisms involve vertical shear of crosswind velocity. For a "cell-shearing" mechanism, shear over the entire vertical extent of the full-depth Langmuir cell is the determining factor, whereas for an 'attraction' mechanism, mid–water column shear is most relevant. Figure 10(b) presents profiles of mean crosswind velocity for the records within the LS event of session 17. During the supercell event, shear of crosswind velocity at mid–water column (dashed level in Fig. 10b) is small when crosswind velocity is large; thus, the "attraction"

mechanism is not likely relevant here. Kukulka et al. (2011) evaluate the importance of the other cell shearing mechanism using a ratio

$$\frac{T_{ad}}{T_{LC}} = \frac{v_{LC}}{H} \left(\frac{\partial V}{\partial Z} \right)^{-1} \tag{1}$$

of crosswind advective timescale T_{ad} to a Langmuir timescale where v_{LC} is a characteristic Langmuir cell velocity, taken as u_*. Assuming crosswind velocity varies linearly from zero at the bottom to V_o near the surface, the timescale ratio calculated using a typical maximum R2 tidal velocity of $V_o \sim 0.3$ m s^{-1} and $u_* \sim 0.2$ m s^{-1} calculated from maximum wind stress τ of ~ 0.4 N m^2 during the LS event of session 17 is $T_{ad}/T_{LC} \sim \frac{u_*}{V_o} \sim 0.6 < 1$, suggesting that cell shearing is a possible explanation for the modulation of LS characteristics at tidal periods. Figure 10(b) shows that over the full water column (or at least that part of it that the observations access), records exhibiting both LS diagnostics are associated with less than maximum values of vertical shear in crosswind velocity. Water column crosswind shear is quite variable through the tidal cycle but at maximum ebb (see Fig. 10a) ranges from 0.8 to 1.3 s^{-1}, depending on whether the high shear bottom boundary layer is included. This is similar to the shear magnitude explored by Kukulka et al. (2011) for episodes of Langmuir cell disruption by cell shearing. At maximum flood, shear values are much lower, ~ 0.5 s^{-1}. However, Figure 10(b) also shows that one LS diagnostic (near-bottom nose, records coded yellow) is found alone in association with near-maximum positive crosswind velocities, thus shear, and the other (maximum $\overline{\langle w'^2 \rangle}$, records coded blue) is found alone with near-maximum negative crosswind velocities. Both diagnostics appear at even lower shear values during the tidal phase between maximum ebb and maximum flood, but neither appears at equally low crosswind shear values between maximum flood and maximum ebb. The crosswind velocity profile alone does thus not predict disruption of strong Langmuir characteristics in a given record: there are many records (crosses in Fig. 10b) with weak LS characteristics but shear structure similar to records with strong LS characteristics.

iii. Diurnal cycle in buoyancy flux. Possible modulation of LS characteristics by addition of convective turbulence is suggested by modifications in apparent period seen in the wavelet analysis of Figure 7 and by peaks in $\langle w'^2 \rangle$ coincident with some (though not all) night-time periods of surface heat loss (positive Q in Fig. 11). Recent LES results of Walker, Tejada-Martínez, and Grosch (2016) for combined Langmuir/buoyancy forcings indicate that for turbulent kinetic energy generation by unstable convection to dominate Langmuir production requires a Rayleigh number ($Ra_\tau \propto Q/u_*^2 \sim 1,000$) that corresponds to surface heat loss greatly in excess of that seen at either LEO or R2. A run with a more modest value of $Ra_\tau \sim 200$ that corresponded to typical LS conditions at LEO exhibited very minor modulation of LS characteristics. Although maximum nocturnal heat loss at R2 during LS events is nearly double that of LEO, so is u_*, so the value of $Ra_\tau \propto Q/u_*^2$ calculated for R2 is only ~ 100. On the basis of the LES results, we would thus expect that unstable convection would produce a negligible effect on LSs at R2. Despite that expectation, the diurnal

cycle in surface heat flux forcing seems the only process likely to produce the minor, but observable, diurnal modulation of LS structures at R2, with the caveat that elevated $\overline{\langle w'^2 \rangle}$ is not observed every night. The magnitude of the effect of destabilizing surface buoyancy flux may depend on the underlying degree of organization of LSs, with the generally weaker, less organized cells at R2 being more sensitive to convection than the highly organized structures typical of LEO that were used in the simulations of Walker, Tejada-Martínez, and Grosch (2016).

5. Conclusions

Analysis of VADCP and auxiliary data at the R2 tower on the Georgia shelf has demonstrated the existence of LSs at a shelf site of nearly twice the water depth at LEO where they were first identified, described, and modeled. The range of identifying features include large water column backscatter (Figs. 2 and 3), appropriately phased backscatter and three-dimensional velocity structure (Figs. 4 and 5), normal and shear stress profiles, and Lumley traces consistent with those seen in LEO observations and in modeling diagnoses (Figs. 6 and 7). The turbulent structures are inferred to be elongate in the downwind/wave direction, based on wavelet analysis that shows variation in apparent period that is consistent with the advection of quasi-steady structures being advected past the VADCP by the crosswind component of tidal (geostrophic mean plus tide) velocity. This conclusion still stands if the direction of elongation is instead nearer that of the geostrophic mean current. In that case, the actual cell spacing would be slightly less (by a factor of $\cos \alpha$, where α is the angle between the wind and the actual elongate direction, between the directions of wind and current) than the ~ 90 m estimated assuming structures aligned with the wind.

Despite identification as LSs, the structures at R2 are less organized than those at LEO, as seen in Figure 3 and in the need for conditional averaging (Figs. 4 and 5) to clearly see ordered relationships between velocity components. Significant modulation of diagnostic elements in time is also consistent with relatively weaker structures at R2.

A number of mechanisms that could contribute to the relative weakness and disorganization of LS structures and/or to their observed tidal and diurnal time dependence have been examined. Because the only contributing forcing with a diurnal period is the buoyancy flux, the relatively small diurnal effects observed seem necessarily attributable to this modulation in forcing. LESs examining the effect of unstable convection on LSs (Walker, Tejada-Martínez, and Grosch 2016) report only weak effects for values of surface heat loss and of $\lambda/H \sim 6$ typical of LEO. We hypothesize that LESs run with the smaller value of $\lambda/H \sim 3$, and hence the weaker structures characteristic of R2, would exhibit larger effects for the same values of surface heat loss. However, this potential explanation for measurable variation at diurnal period relies on preexisting weakness of the LSs that interact with buoyancy-driven motions. We suggest that the closeness of the R2 case to marginal stability of vortex pairs as derived by Rosenhead (1929) offers a fundamental explanation for this underlying weakness (and for the LES results for $\lambda/H \sim 3$ discussed in Section 4a.ii).

The remaining variability at tidal periods has many puzzling features: noses can appear when crosswind velocity and/or shear is both small and large but do not necessarily appear at the same phase on every tide; moreover, there can be significant temporal separation between the appearance of noses and maxima in vertical velocity variance. From the observations alone, it is not clear how any of the mechanisms (Sections 4a.iii and 4b.ii) would (alone or together) produce the observed tidal variability in LS characteristics. Progress in understanding the relative importance of these mechanisms will probably require not only the use of coastal LES models able to simulate a complex of time-mean flows plus time-dependent tidal flows, but also further observations to fill two major gaps in the present measurements. First, it seems essential to obtain concurrent direct observation of the horizontal scale and orientation of LSs, as well as changes in both features with time: either side-scan sonar (Thorpe and Hall 1983; Zedel and Farmer 1991) or fan-beam Doppler (Kukulka et al. 2011) could provide this information. Equally essential but much more difficult to obtain are measurements of velocity shear near the surface.

The direct measurements of LSs at 26 m depth reported here indicate they are not strictly an inner shelf phenomenon. Approximately half of the SAB is 27 m depth or less (Jahnke et al. 2008): the underlying sediments of this large area can thus be affected in typical storms. Furthermore, satellite imagery of ocean color suggests the entire SAB shelf, to the 60 m shelf edge, may be affected at times (Savidge et al. 2008). The areal extent that may be affected by LSs on other shelves will depend on shelf depths, level of stratification, and the imposed wind/wave forcing. The documented existence of LSs at a midshelf location of the SAB, and hence their influence on shelf sediment horizontal transport over a significant fraction of this admittedly shallow but quite wide shelf, argues for a more concerted effort to quantify the forcing conditions and depths to which such events occur on shallow shelves worldwide.

APPENDIX

For the large tidal velocities on the Georgia shelf, it is important to establish that a spectral gap exists between the wave-band velocities and those associated with lower-frequency structures such as Langmuir cells, whose apparent frequency depends on their crosswind width and the speed at which they are advected past the stationary instrument measuring them. If the high-frequency end of Langmuir cell variance overlaps the low-frequency end of the wave spectrum, simple filtering will be insufficient to remove wave variance from the 10 s filtered data. Either some part of the wave energy will remain, or some part of the turbulent structure could be filtered out along with the waves. If such overlap only occurred

when advection of Langmuir cells was fastest, temporal variability in the velocity variances would result. To eliminate these possibilities, spectra are calculated of hourly subsets of mid–water column vertical velocity (bin 10, at 10.6 meters above bottom [mab]) and near-bottom horizontal velocities (bin 3, at 4.0 m mab), rotated into a wind-aligned coordinate system. Vertical velocity variance is highest in mid–water column, while along-wind horizontal velocities are most energetic near bottom for Langmuir supercells, as shown in Section 3b. Spectra for the 1 Hz data (3,600 data points in each hour-long segment) are calculated using Welch's overlapping segment method, with five 50% overlapping segments, each tapered with a Hanning filter. Variance conserving spectra are then integrated over frequency band, and plotted by phase of tide, relative to the beginning of record 46 in session 17 (e.g., Fig. 12), which is approximately at max ebb.

To illustrate overall variability, spectra from bin 10 vertical velocity are shown for every hour during the event illustrated in Figure 3, starting with session 17, record 46, and continuing through session 18, record 3 with each half of each 2 h record analyzed separately (Fig. A1a). A range of low variability exists between 0.03 and 0.07 Hz, to the left of the high-energy wave band on the right. The mean and standard deviation of these spectra by frequency (Fig. A1b) also show low energy and low variability in this apparent gap between waves and lower frequency (longer than ∼1 min period) processes. For reference, Figure A1(b) also shows the standard deviation by frequency of hourly spectra calculated from the filtered data to show where the cutoff for that filtering resides. Means and standard deviations of horizontal wind-coordinate velocity (bin 10) spectra by frequency (Fig. A1c and d) also show low energy and low variability in this apparent gap between waves and lower-frequency processes. Thus, the filter effectively removes wave energy from the velocity data.

To ensure no part of the energy to the left of the spectral gap is filtered out as the advection velocity changes, we examine variability as a function of M2 tidal phase. In Section 3c, we infer that the features detected are wind elongate, consistent with advection past the vertical beam acoustic Doppler current profiler by the crosswind component of the tide plus low-frequency mean velocity. Because of the orientation and magnitude of the low-frequency mean, the mean plus tidal (what we refer to as tidal) crosswind magnitude peaks only once during every semidiurnal cycle (Figs. 9 and 10). This is also demonstrated here by hourly averages of horizontal wind-coordinate velocities versus phase of the M2 tide (Fig. A2), relative to the start of record 46 in session 17, when the tide is oriented approximately seaward (Fig. 10a).

Depth-averaged (bin 3 to the maximum slant bin depth $0.85H$, black) and near-bottom (bin 3, gray) hourly mean values of along-wind (Fig. A2a, positive downwind) and crosswind (Fig. A2b, positive seaward) horizontal velocities are approximately equivalent, reflecting the fact that there is very little mean vertical shear in horizontal velocity throughout this event. Note that the crosswind velocity component is rarely negative, consistent with Figure 9, middle panels, and with the apparent 12.4 h periodicity in dominant frequency in the wavelet analysis (Fig. 8).
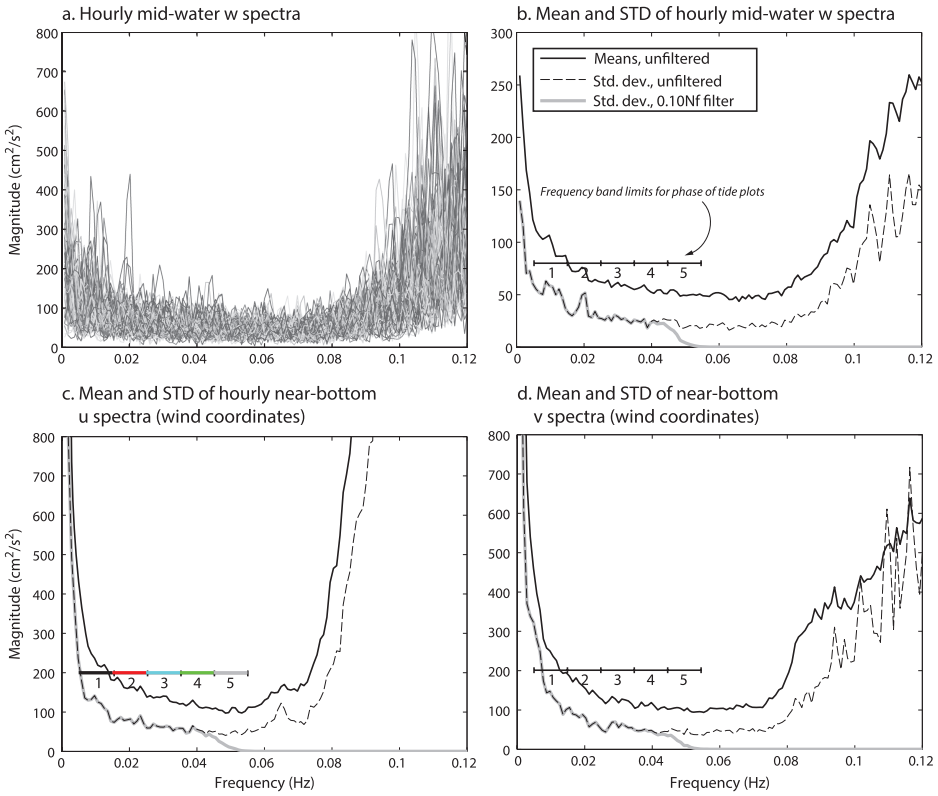
a. Hourly mid-water w spectra

b. Mean and STD of hourly mid-water w spectra

c. Mean and STD of hourly near-bottom
u spectra (wind coordinates)

d. Mean and STD of near-bottom
v spectra (wind coordinates)

Figure A1. Velocity spectra for session 17, records 46–84, and session 18, records 1–3. (a) Spectra for w', fifth beam, bin 10 (10.6 meters above bottom [mab]), from unfiltered hour-long time series. (b) Mean (solid line) and standard deviation (STD; dashed line) of spectra in panel (a), as functions of frequency and STD (gray line) of spectra of filtered w' bin 10 data. (c) Same as in panel (b), but for downwind near-bottom (bin 3, 4.0 mab) horizontal velocity. (d) As in panel (b), but for crosswind near-bottom (bin 3, 4.0 mab) horizontal velocity. In panel (b), the numbered horizontal bars indicate the frequency bands over which averages of each spectrum shown in panel (a) are taken. Similar frequency bands are marked in panels (c) and (d), indicating identical frequency band averages for the horizontal velocity spectra. Nf, Nyquist frequency.

Frequency band integrals of hourly spectral estimates for vertical (bin 10, Fig. A2c) and horizontal velocities (bin 3, Figure A2d and e) are shown. Note first that averages over frequency bands immediately above and below the low-pass filter cutoff frequency show essentially no variation with phase of tide, in either vertical or horizontal velocities (Fig. A2c–e), green and gray, corresponding to the frequency bands numbered 4 and 5 in Figure A1. This illustrates that the spectral gap between waves and the lower-frequency variability is not breached during the period when crosswind water column velocities are
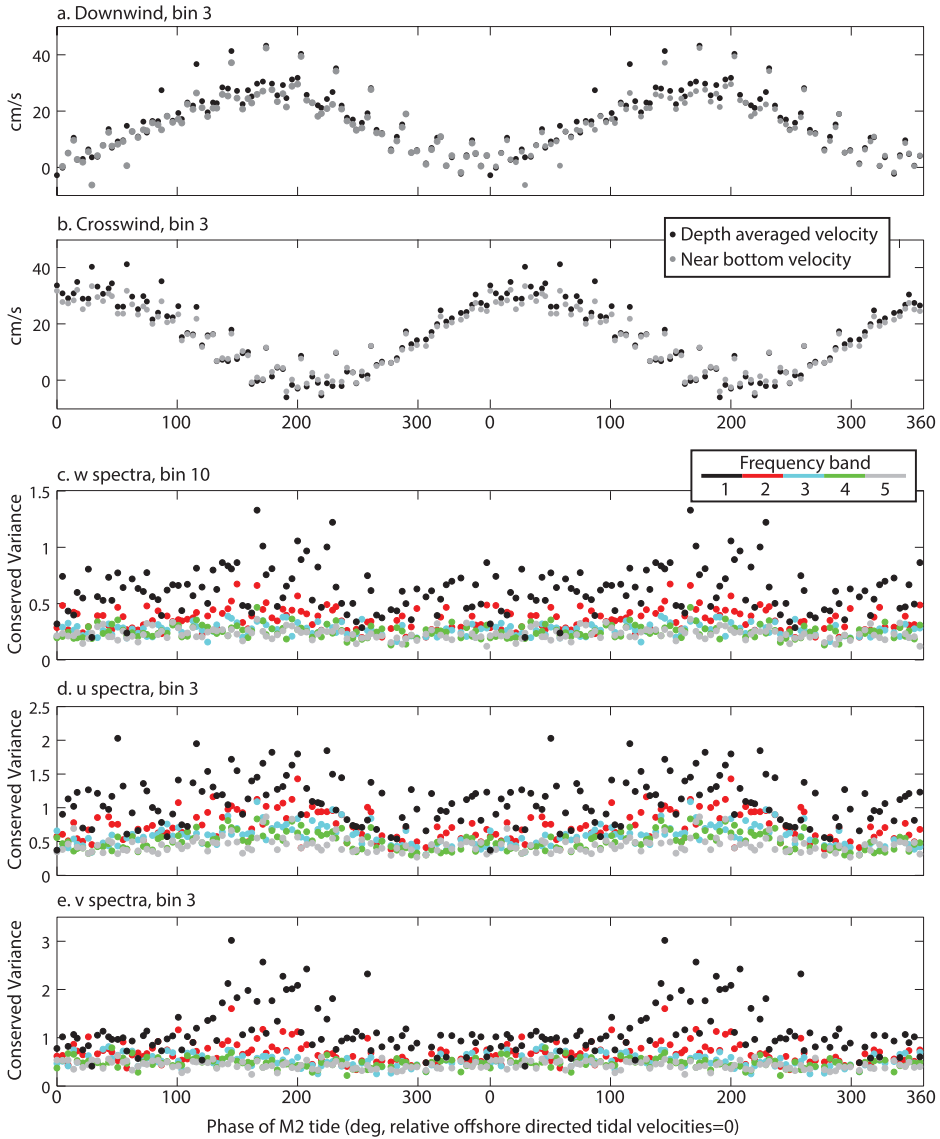
Figure A2. Velocities and velocity spectra plotted as functions of the phase of the tide relative to the start of session 17, record 46. Results for phases 0° to 360° are repeated, plotted also 360° to 720°. (a) Hourly averages of depth-averaged (black circles) and near-bottom (gray circles; bin 3, 4 meters above bottom [mab]) along-wind velocity. (b) As in panel (a), but for crosswind velocity. (c) Frequency band integrations of variance conserving spectra of w' (fifth beam, bin 10, 10.6 mab); colors correspond to the numbered bands in Figure A1. (d) As in panel (c), but for along-wind near-bottom (bin 3, 4 mab) horizontal velocity spectra. (e) As in panel (c), but for crosswind near-bottom (bin 3, 4 mab) horizontal velocity spectra.

largest (Fig. A2b). Frequency band 3 (blue) below the filter cutoff frequency also shows essentially no variation with phase of the tide.

Instead, the tidal variation discussed in Section 3d is clear in frequency bands well below the filter cutoff, from 0.005 to 0.025 Hz (Fig. A2c–e, black and red, corresponding to the frequency bands numbered 1 and 2 in Fig. A1). The frequency band-averaged, variance-conserving spectra of vertical velocity are largest (Fig. A2c, red and black) when crosswind horizontal velocities are smallest (Fig. A2b) and just after downwind velocities peak (Fig. A2a). Near-bottom along-wind and crosswind velocity spectra also show a strong tidal variation, especially the crosswind component (Fig. A2d and e, red and black, note differing y-axis scales).

REFERENCES

Bishop, C. T., and M. A. Donelan. 1987. Measuring waves with pressure transducers. Coastal Eng., *11*(4), 309–328. doi: 10.1016/0378-3839(87)90031-7

Cahoon, L. B., R. A. Laws, and C. J. Thomas. 1994. Viable diatoms and Chlorophyll *a* in continental slope sediments off Cape Hatteras, North Carolina. Deep Sea Res., Part II, *41*(4–6), 767–782. doi: 10.1016/0967-0645(94)90047-7

Craik, A. D. D., and S. Leibovich. 1976. A rational model for Langmuir circulations. J. Fluid Mech., *73*, 401–426. doi: 10.1017/S0022112076001420

Dartus, D., M. Araujo, P. Maurel, and L. Masbernat. 2000. On the influence of longitudinal mean flow over Langmuir circulations. J. Hydraul. Res., *38*(2), 141–149. doi: 10.1080/00221680009498349

Fairall, C. W., E. F. Bradley, D. P. Rogers, J. B. Edson, and G. S. Young 1996. Bulk parameterization of air-sea fluxes for Tropical Ocean-Global Atmosphere Coupled-Ocean Atmosphere Response Experiment. J. Geophys. Res.: Oceans, *101*(C2), 3747–3764. doi: 10.1029/95JC03205

Gargett, A., J. Wells, A. E. Tejada-Martínez, and C. E. Grosch. 2004. Langmuir supercells: A mechanism for sediment resuspension and transport in shallow seas. Science, *306*(5703), 1925–1928. doi: 10.1126/science.1100849

Gargett, A. E., and C. E. Grosch. 2014. Turbulence process domination under the combined forcings of wind stress, the Langmuir vortex force, and surface cooling. J. Phys. Oceanogr., *44*(1), 44–67. doi: 10.1175/JPO-D-13-021.1

Gargett, A. E., D. K. Savidge, and J. R. Wells. 2014. Anatomy of a Langmuir supercell event. J. Mar. Res., *72*(3), 127–163. doi: 10.1357/002224014814901976

Gargett, A. E., A. E. Tejada-Martínez, and C. E. Grosch. 2009. Measuring turbulent large-eddy structures with an ADCP. Part 2. Horizontal velocity variance. J. Mar. Res., *67*(5), 569–595. doi: 10.1357/002224009791218823

Gargett, A. E., and J. R. Wells. 2007. Langmuir turbulence in shallow water. Part I. Observations. J. Fluid Mech., *576*, 27–61. doi: 10.1017/S0022112006004575

Gnanadesikan, A., and R. A. Weller. 1995. Structure and instability of the Ekman spiral in the presence of surface gravity waves. J. Phys. Oceanogr., *25*, 3148–3171. doi: 10.1175/1520-0485(1995)025%3C3148:SAIOTE%3E2.0.CO;2

Grosch, C. E., and A. E. Gargett. 2016. Why do LES of Langmuir supercells not include rotation? J. Phys. Oceanogr., *46*(12), 3595–3597. doi: 10.1175/JPO-D-16-0092.1

Jahnke, R. A., J. R. Nelson, M. E. Richards, C. Y. Robertson, A. M. F. Rao, and D. B. Jahnke. 2008. Benthic primary productivity on the Georgia midcontinental shelf: Benthic flux measurements and high-resolution, continuous in situ PAR records. J. Geophys. Res.: Oceans, *113*, C08022. doi: 10.1029/2008JC004745

Kirincich, A. R. and J. H. Rosman. 2011. A comparison of methods for estimating Reynolds stress from ADCP measurements in wavy environments. J. Atmos. Oceanic Technol., *28*(22), 1539–1553. doi: 10.1175/JTECH-D-11-00001.1

Kosro, P. M. 1985. Shipboard Acoustic Current Profiling during the Coastal Ocean Dynamics Experiment. PhD diss. La Jolla, CA: University of California, San Diego/Scripps Institute of Oceanography, 20 pp.

Kukulka, T., A. J. Plueddemann, J. H. Trowbridge, and P. P. Sullivan. 2011. The influence of crosswind tidal currents on Langmuir circulation in a shallow ocean J. Geophys. Res.: Oceans, *116*, C08005. doi: 10.1029/2011JC006971

Langmuir, I. 1938. Surface motion of water induced by wind. Science, *87*(2250), 119–123. doi: 10.1126/science.87.2250.119

Large, W. G., and S. Pond. 1981. Open ocean momentum flux measurements in moderate to strong winds. J. Phys. Oceanogr., *11*(3), 324–336. doi: 10.1175/1520-0485(1981)011%3C0324: OOMFMI%3E2.0.CO;2

Leibovich, S. 1983. The form and dynamics of Langmuir circulations. Ann Rev. Fluid Mech., *15*, 391–427.

Li, M., C. Garrett, and E. Skyllingstad. 2005. A regime diagram for classifying turbulent large eddies in the upper ocean. Deep Sea Res., Part I, *52*(2), 259–278. doi: 10.1016/j.dsr.2004.09.004

Lohrmann, A., B. Hackett, and L. P. Røed. 1990. High resolution measurements of turbulence, velocity and stress using a pulse-to-pulse coherent sonar. J. Atmos. Oceanic Technol., *7*(1), 19–37. doi: 10.1175/1520-0426(1990)007%3C0019:HRMOTV%3E2.0.CO;2

Martinat, G., Y., Xu, C. E. Grosch, and A. E. Tejada-Martínez. 2011. LES of turbulent surface shear stress and pressure-gradient-driven flow on shallow continental shelves. Ocean Dyn., *61*, 1369. doi: 10.1007/s10236-011-0450-3

McGee, D., R. A. Laws, and L. B. Cahoon. 2008. Live benthic diatoms from the upper continental slope: Extending the limits of marine primary production. Mar. Ecol. Prog. Ser., *356*, 103–112. doi: 10.3354/meps07280

Miles, T., S. M. Glenn, and O. Schofield. 2013. Temporal and spatial variability in fall storm induced sediment resuspension on the Mid-Atlantic Bight. Cont. Shelf Res., *63*, S36–S49. doi: 10.1016/j.csr.2012.08.006

Nelson, J. R., J. E. Eckman, C. Y. Robertson, R. L. Marinelli, and R. A. Jahnke. 1999. Benthic microalgal biomass and irradiance at the sea floor on the continental shelf of the South Atlantic Bight: Spatial and temporal variability and storm effects. Cont. Shelf Res., *19*(4), 477–505. doi: 10.1016/S0278-4343(98)00092-2

Pawlowicz, R., R. Beardsley, S. Lentz, E. Dever, and A. Anis. 2001. Software simplifies air-sea data estimates. EOS, Trans. Am. Geophys. Union, *82*(1), 2. doi: 10.1029/01EO00004

Pope, S. B. 2000. Turbulent Flows. Cambridge: Cambridge University Press, 771pp.

Rosenhead, L. 1929. The Kármán street of vortices in a channel of finite breadth. Philos. Trans. R. Soc., A, *228*, 275–329.

Savidge, W. B., A. Gargett, R. A. Jahnke, J. R. Nelson, D. K. Savidge, R. T. Short, and G. Voulgaris. 2008. Forcing and dynamics of seafloor-water column exchange on a broad continental shelf. Oceanography, *21*(4), 179–184.

Scully, M. E., A. W. Fisher, S. E. Suttles, L. P. Sanford, and W. C. Boicourt. 2015. Characterization and modulation of Langmuir circulation in Chesapeake Bay. J. Phys. Oceanogr., *45*(10), 2621–2639. doi: 10.1175/JPO-D-14-0239.1

Seim, H. E. 2000. Implementation of the South Atlantic Bight Synoptic offshore observational network. Oceanography, *13*(2), 18–23. doi: 10.5670/oceanog.2000.29

Smith, S. D. 1988. Coefficients for sea surface wind stress, heat flux, and wind profiles as a function of wind speed and temperature. J. Geophys. Res.: Oceans, *93*(C12), 15467–15472. doi: 10.1029/JC093iC12p15467

Tejada-Martínez, A. E., and C. E. Grosch. 2007. Langmuir turbulence in shallow water. Part 2. Large-eddy simulation. J. Fluid Mech., *576*, 63–108. doi: 10.1017/S0022112006004587

Thorpe, S. A. 1992. The breakup of Langmuir circulation and the instability of an array of vortices. J. Phys. Oceanogr., *22*(4), 350–360. doi: 10.1175/1520-0485(1992)022%3C0350:TBOLCA%3E2.0.CO;2

Thorpe, S. A., and A. J. Hall. 1983. The characteristics of breaking waves, bubble clouds, and near-surface currents observed using side-scan sonar. Cont. Shelf Res., *1*(4), 353–384. doi: 10.1016/0278-4343(83)90003-1

Trowbridge, J. H., and Y. C. Agrawal. 1995. Glimpses of a wave boundary layer. J. Geophys. Res.: Oceans, *100*(C10), 20729–20743. doi: 10.1029/95JC02131

Walker, R., A. E. Tejada-Martínez, and C. E. Grosch. 2016. Large-eddy simulation of a coastal ocean under the combined effects of surface heat fluxes and full-depth Langmuir circulation. J. Phys. Oceanogr., *46*(8), 2411–2436. doi: 10.1175/JPO-D-15-0168.1

Zedel, L., and D. M. Farmer. 1991. Organized structures in subsurface bubble clouds: Langmuir circulation in the open ocean. J. Geophys. Res.: Oceans, *96*(C5), 8889–8900. doi: 10.1029/91JC00189